

PERFORMANCE EVALUATION OF A SMALL FIELD-OF-VIEW, MOBILE
PET/SPECT SYSTEM

By

MATTHEW THOMAS STUDENSKI

A THESIS PRESENTED TO THE GRADUATE SCHOOL
OF THE UNIVERSITY OF FLORIDA IN PARTIAL FULFILLMENT
OF THE REQUIREMENTS FOR THE DEGREE OF
MASTER OF SCIENCE

UNIVERSITY OF FLORIDA

2008

© 2008 Matthew Thomas Studenski

TABLE OF CONTENTS

	<u>page</u>
LIST OF TABLES	5
LIST OF FIGURES	6
ABSTRACT	10
CHAPTER	
1 THE MOBILE PET/SPECT SYSTEM	12
Purpose of the System	12
Nuclear Medicine.....	12
Clinical Uses for PET and SPECT	13
Benefits of the Mobile System’s Design	15
2 SYSTEM DESIGN	16
Detectors	16
Gantry	16
Detector Positioning	17
3 SYSTEM EVALUATION METHODS	23
Introduction.....	23
Intrinsic Energy Resolution	23
Spatial Resolution.....	23
Detection Sensitivity.....	25
Count Rate Capability.....	26
4 SYSTEM EVALUATION RESULTS	28
Intrinsic Energy Resolution	28
Spatial Resolution.....	28
Detection Sensitivity.....	30
Count Rate Capability.....	30
5 DYNAMIC CARDIAC PHANTOM STUDIES	35
Introduction.....	35
Methods	35
Results.....	36
Discussion.....	37
6 CONCLUSIONS AND FUTURE WORK	42

LIST OF REFERENCES43
BIOGRAPHICAL SKETCH44

LIST OF TABLES

<u>Table</u>		<u>page</u>
3-1	Low Energy (140 keV) and High Energy (511 keV) Collimator Parameters.....	27
4-1	System Spatial Resolution (FWHM in cm).	34
5-1	Myocardium to Ventricle Intensity Ratios for Different Acquisition Parameters.....	41

LIST OF FIGURES

<u>Figure</u>	<u>page</u>
2-1 Various views of the mobile PET/SPECT imaging system. Detectors are shown in A) AP orientation. B) Left lateral and right anterior oblique orientation. C) Lateral orientation.	19
2-2 Front view of the associated electronics rack and computers for the mobile system.	19
2-3 View of the detector head showing the 4×4 photomultiplier tube array and pixilated NaI crystal.	19
2-4 Two views of a typical ICU patient bed. Note that the side rails are adjustable.	20
2-5 Computer-aided design drawings of the system gantry and the different detector positioning capabilities. A) Anterior-posterior orientation. B) Lateral orientation. C) Oblique and posterior orientation. D) Oblique and posterior orientation.	20
2-6 A single detector head fitted with a collimator can be used for single photon imaging to achieve complete angular sampling which might not be able to be achieved with a detector underneath the bed in PET mode.	21
2-7 Illustration of how a center-of-rotation shift causes the position of the image to change (axis of rotation is located between the arrows). A) No center-of-rotation shift. B) Center-of-rotation shift.	22
3-1 Cross-section of a parallel-hole collimator with different parameters labeled (not to scale).	26
4-1 Energy spectra from flood images with two different point sources. A) ^{99m} Tc energy spectrum. B) ¹⁸ F-FDG energy spectrum.	31
4-2 Normalized intrinsic spatial resolution LSFs. A) ^{99m} Tc LSF. B) ¹⁸ F-FDG LSF.	31
4-3 Normalized system spatial resolution LSFs at 10, 20, and 30 cm from the detector face in both the x and y directions. A) ^{99m} Tc LSF in the x direction. B) ¹⁸ F-FDG LSF in the x direction. C) ^{99m} Tc LSF in the y direction. D) ¹⁸ F-FDG LSF in the y direction.	32
4-4 Line source images for system spatial resolution measurements. Line source to detector distance was 10 cm. A) ^{99m} Tc line source. B) ¹⁸ F-FDG line source.	32
4-5 Acquired and simulated 511 keV point source images with the corresponding normalized PSFs in the x and y directions. A) Acquired point source. B) Simulated point source.	33

4-6	Reconstructed transaxial slice from a SPECT image from a ^{99m}Tc point source with its corresponding point spread functions in the transaxial and coronal directions.	33
4-7	Reconstructed transaxial slice from a SPECT image from an ^{18}F point source with its corresponding point spread functions in the transaxial and coronal directions.	34
4-8	Count rate as a function of activity. A) ^{99m}Tc counting curve. B) ^{18}F -FDG counting curve.....	34
5-1	Dynamic cardiac phantom with simulated myocardium, lungs, spine, and liver.	39
5-2	^{99m}Tc end-diastole and end-systole reconstructions from 19 projection angles and 2.5×10^5 counts per projection with the corresponding profile. A) End-diastole reconstruction. B) End-systole reconstruction.....	39
5-3	Transaxial and coronal slices using ^{99m}Tc with varying number of projection angles with 2.5×10^5 counts per projection with both cardiac motion and out-of-field activity in the liver. A) 19 projection angles. B) 10 projection angles. C) 5 projection angles.	40
5-4	Transaxial and coronal slices using ^{18}F -FDG with varying number of projection angles with 2.5×10^5 counts per projection with cardiac motion, only. A) 19 projection angles. B) 10 projection angles. C) 5 projection angles.	40
5-5	Projection at $\theta = 45^\circ$ showing that the detector can be located at any position to achieve the best image while at the same time eliminating center-of-rotation artifacts and truncation of anatomy.	41

LIST OF ABBREVIATIONS

PET	Positron Emission Tomography
SPECT	Single Photon Emission Computed Tomography
ICU	Intensive Care Unit
ER	Emergency Room
CT	Computed Tomography
^{18}F	Fluorine-18
FDG	Fluoro-deoxy Glucose
keV	Kilo Electronvolt
$^{99\text{m}}\text{Tc}$	Technetium-99 Metastable
cm	Centimeter
mm	Millimeter
m	Meter
in	Inch
NaI(Tl)	Sodium Iodine doped with Thallium
GSO	Gadolinium Orthosilicate
LSO	Lutetium Orthosilicate
PMT	Photomultiplier Tube
μCi	Microcurie
mCi	Millicurie
FWHM	Full Width at Half Maximum
^{57}Co	Cobalt-57
^{137}Cs	Cesium-137
d	Collimator Hole Diameter
a	Collimator Hole Depth

b	Source-to-Collimator Distance
a_{eff}	Effective Collimator Hole Depth
μ	Attenuation Coefficient
R_c	Collimator Resolution
g	Collimator Sensitivity
MLEM	Maximum Likelihood Expectation Maximum
s	Second
LSF	Line Spread Function
PSF	Point Spread Function
BPM	Beats per Minute
EF	Ejection Fraction
ROR	Radius of Rotation

Abstract of Thesis Presented to the Graduate School
of the University of Florida in Partial Fulfillment of the
Requirements for the Degree of Master of Science

PERFORMANCE EVALUATION OF A SMALL FIELD-OF-VIEW, MOBILE
PET/SPECT SYSTEM

By

Matthew Thomas Studenski

May 2008

Chair: David Gilland

Major: Nuclear Engineering Sciences

This thesis reports on the initial performance evaluation of a bedside cardiac SPECT system. The system was designed to move within a hospital to image critically-ill patients, for example, those in intensive care unit (ICU) or emergency room settings, who cannot easily be transported to a conventional SPECT or PET facility. The performance is evaluated for both 140 keV (^{99m}Tc) and 511 keV (^{18}F -FDG) emitters with the system operating in single photon counting mode. The imaging performance metrics for both 140 keV and 511 keV included intrinsic energy resolution, spatial resolution (planar and reconstructed SPECT), detection sensitivity, and count rate capability. Results demonstrated an intrinsic energy resolution of 32% at 140 keV and 23% at 511 keV, a planar intrinsic spatial resolution of 5.6 mm full width half-maximum (FWHM) at 140 keV and 6.1 mm FWHM at 511 keV, a system spatial resolution at 10 cm of 1.14 cm FWHM for both 140 keV and 511 keV, a reconstructed SPECT spatial resolution of 1.59 cm at 140 keV (20 cm radius-of-rotation), a sensitivity of $3.1 \text{ counts} \cdot \mu\text{Ci}^{-1} \cdot \text{s}^{-1}$ at 140 keV and $0.48 \text{ counts} \cdot \mu\text{Ci}^{-1} \cdot \text{s}^{-1}$ at 511 keV, and a maximum count rate of $1.46 \times 10^5 \text{ counts/s}$ at 140 keV and $1.56 \times 10^5 \text{ counts/s}$ at 511 keV.

To further the study, a dynamic cardiac phantom was used to evaluate the effects of angular sampling, counts per projection, cardiac motion, and out of field activity in bedside SPECT imaging using ^{99m}Tc and ^{18}F -FDG. Collimated ^{18}F -FDG-SPECT imaging is preferred over PET in this environment due to difficulties in positioning a detector beneath a bed. More projection angles with less attenuation effect can be obtained with anterior SPECT as well. Acquisitions were performed at end systole, end diastole, with the heart beating, and with the heart beating and activity in the simulated liver. Viable images were reconstructed using MLEM for both ^{99m}Tc and ^{18}F -FDG. Contrast increases with increased angular sampling and counts per projection in these images. An algorithm is currently being developed to correct for center-of-rotation errors in the SPECT acquisitions to reduce streaking artifacts. Filtering of the ^{18}F -FDG images is also being considered to reduce septal penetration artifacts. SPECT cardiac imaging of immobile, critically ill patients is possible using both ^{99m}Tc and ^{18}F -FDG. The versatility of this system makes it a useful tool for examining patients who could not have this exam but would benefit from it greatly.

CHAPTER 1 THE MOBILE PET/SPECT SYSTEM

Purpose of the System

A mobile, small field-of-view, PET/SPECT system has been designed that can move within a hospital to image critically-ill patients, for example, those in intensive care unit (ICU) or emergency room (ER) settings. Because of their medical condition, these patients cannot easily be transported to a conventional single photon emission computed tomography (SPECT) or positron emission tomography (PET) facility. Currently in the ICU or ER patients with known or suspected severe coronary artery disease typically must be managed without the benefit of myocardial perfusion or viability imaging studies to assess patient condition. Although portable cardiac SPECT systems are currently commercially marketed, for example, the Nomad system by the Segami Corporation, the mobile system here is unique in its design to image critically-ill patients lying in ICU or ER beds without having to move them.

Nuclear Medicine

Positron emission tomography (PET) and single photon emission computed tomography (SPECT) are the backbone of nuclear medicine. Both of these imaging modalities are unique in that they are functional imaging modalities, that is, they can show physiological processes that are occurring in the body and not just anatomical features, as in planar radiography, fluoroscopy, or computed tomography (CT). Typical clinical PET systems are made up of a ring of scintillation detectors that surround the patient. Before the scan, the patient is injected with a positron emitter, typically ^{18}F -fluoro-deoxy-glucose (^{18}F -FDG), which will be metabolized by tissues in the patient. The ^{18}F -FDG (or other compound) will decay, emitting a positron which will undergo an annihilation reaction. Each annihilation reaction produces two 511 keV photons emitted at 180° from each other to conserve momentum. These two photons exit the patient and

are detected in the ring of detectors. By using timing circuits the system can determine the two detectors where the annihilation photons interacted. This is termed a coincidence event and by connecting the two detectors, a line of response can be determined. By recording all of the lines of response, a 3D image can be reconstructed.

In SPECT imaging, the patient is injected with a gamma emitter that will be preferentially uptaken into an organ of interest. The most common is ^{99m}Tc Technetium methoxy isobutyl isonitrile (^{99m}Tc sestamibi), which is uptaken into the myocardium (heart muscle). The gamma ray that is emitted is detected by scintillation detectors that rotate around the patient. The 2D image acquired at each angle is called a projection. To accurately reconstruct a 3D image, at least 180° must be covered by the detectors. Each detector has a lead collimator, typically parallel hole, which only allows gamma rays to interact in the detector from a known line of response. After the detector has obtained enough projection images around the patient, a 3D image can be reconstructed using the known lines of response.

Clinical Uses for PET and SPECT

Clinically, ^{18}F -FDG-PET scans are used most often to detect cancer and to examine the effects of cancer therapy, but this is just the surface of what PET is capable of. The reason for using PET to detect and monitor cancers is that ^{18}F -FDG is a metabolism tracer and cancers, because they can grow rapidly, readily uptake the tagged glucose tracer. These cancer monitoring scans can be whole body or limited to the area of the suspected cancer.

Other uses for PET include brain scans to evaluate patients who have memory disorders of an undetermined cause or seizure disorders that are not responsive to therapy. ^{18}F -FDG-PET imaging also helps evaluate signs of coronary artery disease. PET scans of the heart can be used to determine if areas of the heart that show decreased function are alive or scarred as a result of a prior heart attack or myocardial infarction. Combined with a myocardial perfusion study, PET

scans allow the study of myocardial viability, that is, differentiation of nonfunctioning heart muscle from heart muscle that would benefit from a medical procedure, such as an angioplasty or coronary artery bypass surgery to reestablish adequate blood flow and improve heart function.

Myocardial perfusion imaging is performed most commonly using ^{99m}Tc sestamibi in a SPECT procedure to determine the condition of the patient's myocardium. Typically, the procedure involves two studies of the myocardium: under stress and at rest. In both studies, the patient is injected with ^{99m}Tc , whose uptake is proportional to the instantaneous myocardial perfusion. For the stress study, the patient is subjected to stress, physical or pharmacological, just prior to radiopharmaceutical injection. This is an indicator of perfusion during periods of increased myocardial activity. The rest study is used as an indicator of myocardial viability where low perfusion indicates non-viable tissue and high perfusion indicates viable myocardial tissue that can be revascularized. Regions of the myocardium that show reduced blood flow in the stress test but appear normal in the rest study are termed ischemic.

Along with ^{99m}Tc sestamibi myocardial perfusion imaging, ^{18}F -FDG-PET is a form of myocardial metabolic imaging. ^{18}F -FDG-PET imaging shows the measure of regional glucose metabolism and is used to determine the viability of cardiac tissue, not the amount of blood flowing through it. A study of 37 patients (185 myocardial segments) has shown that although sestamibi and ^{18}F -FDG measures of myocardial viability are often comparable, sestamibi underestimates or overestimates myocardial viability diagnosis in 29% cases as compared to ^{18}F -FDG-PET [1]. This conclusion was confirmed by tracking post-operative improvement in patients' condition. This study shows that using only sestamibi as a diagnostic tool for cardiac disease could possibly lead to misdiagnosis.

Another option for myocardial imaging is to use ^{18}F -FDG as the radiotracer but use a SPECT system instead of a PET system. Previous studies on myocardial ^{18}F -FDG-SPECT show that on the basis of regional ^{18}F -FDG uptake and defect scores (a visual four-point scale that indicated the presence of absence of a defect in the left ventricular myocardium), ^{18}F -FDG-SPECT using ultra high energy collimators can be used for assessment of myocardial viability as accurately as ^{18}F -FDG-PET [2]. Using appropriate intensity thresholding, it was shown in phantom studies that ^{18}F -FDG-SPECT can be used to measure defect size as accurately as conventional PET [1]. Based on these prior studies, it can be seen that ^{18}F -FDG-SPECT can be used effectively for myocardial imaging.

Benefits of the Mobile System's Design

Previous studies demonstrate that using only sestamibi for detecting cardiac disease can lead to misdiagnosis. The mobile PET/SPECT system is not limited to only imaging patients injected with sestamibi like currently marketed mobile SPECT systems. This system can image patients in SPECT mode who have been injected with sestamibi and also patients who have been injected with ^{18}F -FDG in either SPECT mode or PET mode. Not only is the system unique in that it can perform both PET and SPECT, but it can perform SPECT at two different energies using two different radioactive tracers. This is of great benefit to patients who are confined to beds and would have to be moved multiple times to different facilities to undergo the same studies. The small field-of-view detectors make this system ideal for imaging not only the heart, but also the brain and other small organs, adding to the types of studies that could be performed on immobile patients.

CHAPTER 2 SYSTEM DESIGN

Detectors

The system consists of two compact detectors, each with approximately $25 \times 25 \text{ cm}^2$ detector areas, mounted on a mobile gantry system with a detachable computer and electronics rack (Figs. 2-1 and 2-2). The electronics rack is 62 cm (24.5 in) deep, 66 cm (26 in) wide, and 1 m (39 in) tall. The detectors (fabricated at Thomas Jefferson National Accelerator Facility [3]) consist of pixilated NaI(Tl) ($5.0 \times 5.0 \times 12.5 \text{ mm}^3$ with 5.5 mm pitch). This scintillator was chosen to enable a compact and economical imager for both $^{99\text{m}}\text{Tc}$ (140 keV) and ^{18}F -FDG and other positron tracers (511 keV). Raylman *et al.* compared the performance of three scintillators: NaI(Tl), GSO and LSO [4]. The NaI(Tl) system produced the best energy resolution but had the worst spatial resolution and lowest detection sensitivity.

In spite of this lower detection efficiency, NaI(Tl) was chosen in this system design due to its lower cost and its superior performance in imaging 140 keV gamma emission. We also anticipate that this low detection efficiency can be partially compensated by longer scan times in ICU applications. The photomultiplier tube (PMT) readout uses position-sensitive PMTs with high-rate four analog outputs arranged in a 4×4 array for each detector to form the $25 \times 25 \text{ cm}^2$ active detector area (Fig. 2-3). A detailed description of the detector electronics and signal processing can be found in [3].

Gantry

The custom manufactured gantry system, manufactured by Accelerated Development Solutions (Phillipsburg, NJ, 08865), has been designed to position the detectors for tomographic imaging under the challenging conditions imposed by the ICU or emergency room settings. Fig. 2-4 shows photographs of a typical ICU bed. The gantry is built on a standard palate jack with 8

cm (3 in) low profile legs that slide beneath ICU beds for stable support, as shown in the computer-aided design drawings in Fig. 2-5. The base is 1.47 m (58 in) long and 75 cm (29.5 in) wide. The detectors mount to the rails of a linear bearing set that allows precise horizontal and vertical detector motion. Vertical detector motion is motor-driven using electronic motion control modules and the horizontal motion is controlled manually. The height of the gantry is 1.97 m (77.5 in). Detector pivoting provides the additional, necessary motion dimension for tomographic imaging. The linear motions and pivot angle are digitally encoded for input to the reconstruction software and can be readout on the gantry.

Detector Positioning

Although this system is capable of acquiring coincidence PET data from the two detectors in opposing orientation (Figs. 2-5A, and 2-5B), the 511 keV SPECT approach, using high energy collimators and acquiring projections over the anterior 180° (Figs. 2-1B and 2-6), has advantages despite the reduced detection sensitivity from the high energy collimators. First, projection data with complete angular sampling (anterior 180°) are more readily achieved with SPECT mode compared with PET mode (Fig. 2-6). The latter mode requires positioning and orbiting a detector beneath the patient bed and it might not be feasible to rotate a detector beneath the bed to achieve full angular sampling due to the obstruction from support structures and the thickness of the mattress [5]. Second, the effects of attenuation and scatter in the patient body are greatly reduced with 511 keV SPECT for cardiac imaging using 180° anterior data relative to PET, which has attenuation effects from the entire thickness of the patient.

For a SPECT acquisition, the position of the head at each projection is defined by three parameters; the head angle, θ , the horizontal position, H , and the vertical position, V . A digital protractor displays the head angle while the horizontal and vertical positions are displayed digitally on the gantry. To simplify the first SPECT acquisitions, a fixed radius-of-rotation

(ROR) was used with the source placed on the axis of rotation. By placing the source directly on the axis of rotation, center-of-rotation shifts can be avoided if a fixed ROR is assumed. A center-of-rotation shift occurs when the axis of rotation does not project exactly to the center of the detector. The result is the projection of the axis changes as the projection angle changes rather than projecting to the center of the detector at all angles. Fig. 2-7 shows an example of a center-of-rotation shift in a 64 pixel detector. Notice that when the detector is in the opposing orientation with a center-of-rotation shift, the axis of rotation projects to the opposite side of the detector. When the final image is reconstructed, any center-of-rotation shifts will create doughnut-like streaking artifacts which degrade the image quality.

Simple trigonometric equations were developed to calculate the horizontal and vertical detector position for each projection angle, assuming a fixed ROR. Equations 2-1 and 2-2 define H and V as a function of θ and a constant ROR in mm. The ROR and number of evenly spaced projection angles are chosen before the acquisition is performed.

$$H = (279)(\text{ROR})(1 - \cos \theta) \quad (2-1)$$

$$V = (288)(\text{ROR})(\sin \theta) \quad (2-2)$$

Center-of-rotation shift is a common occurrence in the clinical setting and can result from electronic components in the detector heads or mechanical issues with the head rotation. It is easily corrected for in the clinic because the shift will be the same for every projection angle. In the bedside environment with this mobile system, there is a possibility for a different center-of-rotation shift in every projection since the detector is manually positioned at each angle. Right now, this issue will be avoided by using the fixed ROR and having the source positioned exactly at the center of the field-of-view. The center-of-rotation issue will be addressed in chapter 5.



Figure 2-1. Various views of the mobile PET/SPECT imaging system. Detectors are shown in A) AP orientation. B) Left lateral and right anterior oblique orientation. C) Lateral orientation.

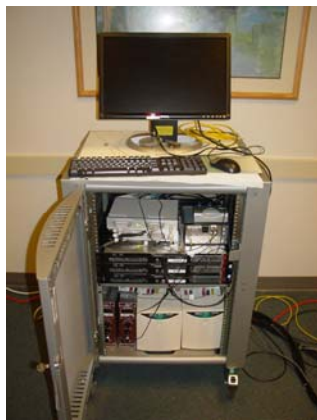


Figure 2-2. Front view of the associated electronics rack and computers for the mobile system.

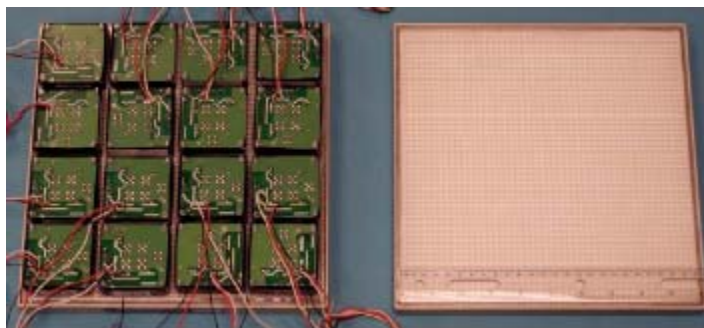


Figure 2-3. View of the detector head showing the 4x4 photomultiplier tube array and pixilated NaI crystal.



Figure 2-4. Two views of a typical ICU patient bed. Note that the side rails are adjustable.

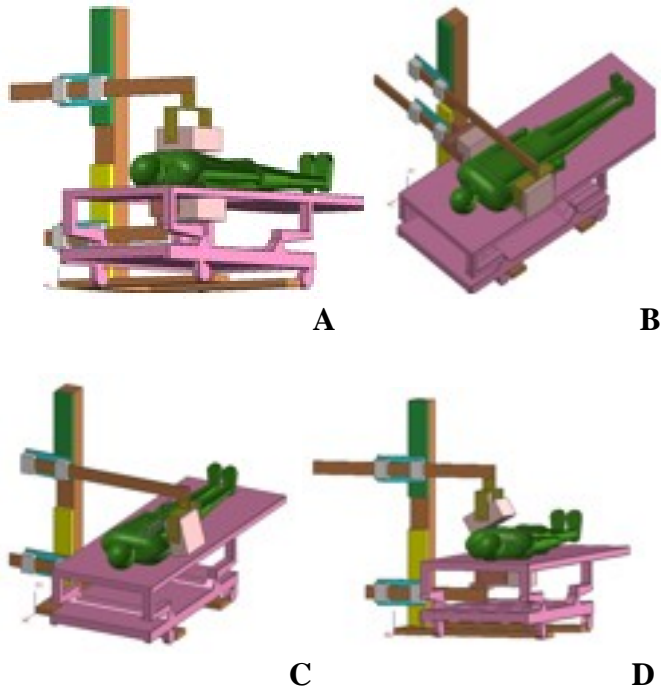


Figure 2-5. Computer-aided design drawings of the system gantry and the different detector positioning capabilities. A) Anterior-posterior orientation. B) Lateral orientation. C) Oblique and posterior orientation. D) Oblique and posterior orientation.

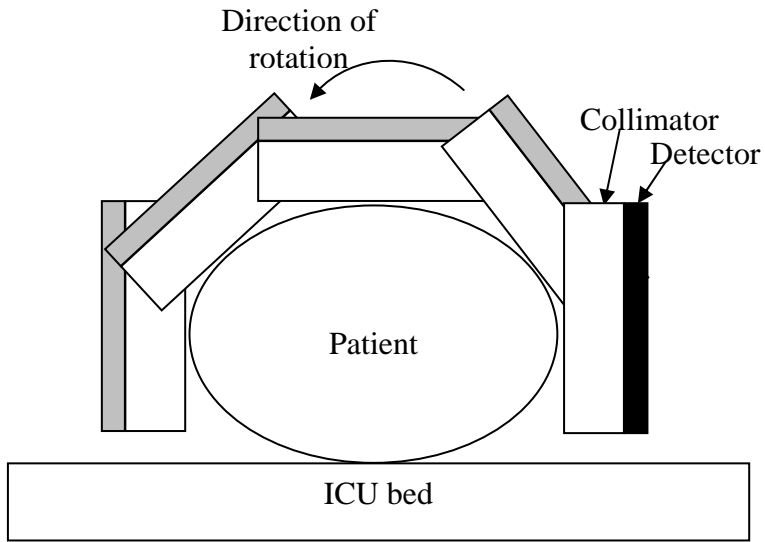


Figure 2-6. A single detector head fitted with a collimator can be used for single photon imaging to achieve complete angular sampling which might not be able to be achieved with a detector underneath the bed in PET mode.

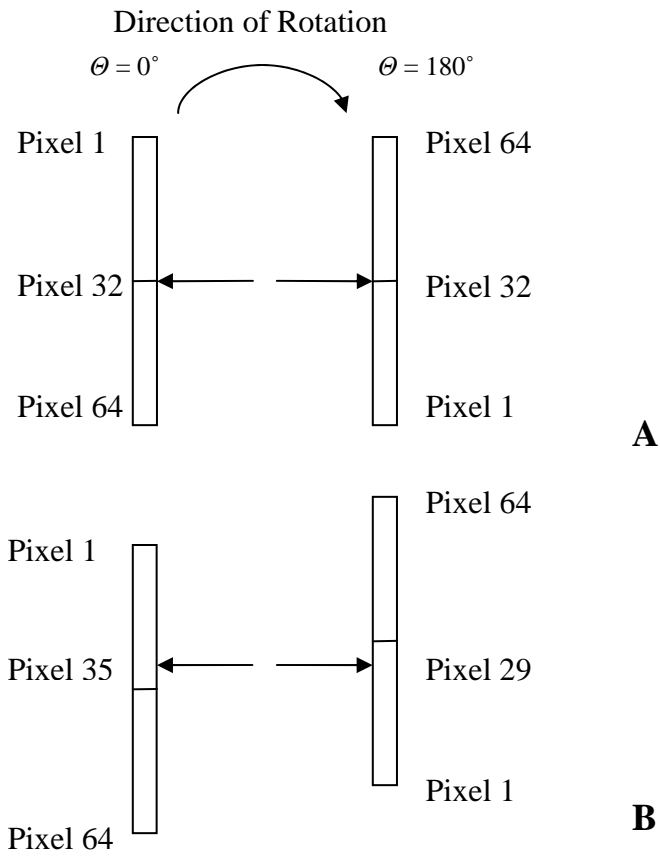


Figure 2-7. Illustration of how a center-of-rotation shift causes the position of the image to change (axis of rotation is located between the arrows). A) No center-of-rotation shift. B) Center-of-rotation shift.

CHAPTER 3 SYSTEM EVALUATION METHODS

Introduction

Four imaging performance metrics were evaluated for both ^{99m}Tc (140 keV) and ^{18}F FDG (511 keV) imaging with this system: intrinsic energy resolution, spatial resolution (planar and reconstructed SPECT), detection sensitivity, and count rate capability.

Intrinsic Energy Resolution

The energy resolution of the system was measured intrinsically (without collimator) with a point source positioned 75 cm from the detector face and 1.0×10^7 total counts acquired for each source. Using this geometry, energy spectra of the point sources were obtained. An 80 μCi source of ^{99m}Tc was imaged at the detector's low energy setting and a 240 μCi source of ^{18}F -FDG was imaged at the high energy setting. These activities were low enough to ensure that the detector did not exceed the maximum count rate. The peak channel and the FWHM of each spectrum were measured.

To determine a keV/channel calibration factor for each energy setting, a 5 μCi source of ^{57}Co (122 keV gamma) was imaged at the low energy setting and a 65 μCi source of ^{137}Cs (662 keV gamma) was imaged at the high energy setting. The peak channel for each of these sources was measured and a keV/channel factor was obtained for each energy setting. This calibration factor was used to convert the measured energy resolution (FWHM in channels) into keV units.

Spatial Resolution

The intrinsic planar spatial resolution of the system at 140 keV and 511 keV was measured using a 1 mm wide slit phantom made from 2 cm thick lead bricks separated by 1 mm spacers and ^{99m}Tc (190 μCi) and ^{18}F -FDG (160 μCi) point sources. The sources were positioned 75 cm from the detector face, and 1×10^7 counts were obtained for both energies. Count rate was

substantially below the system maximum. In order to avoid detector pixelization effects, the intrinsic spatial resolution was measured and averaged over 3 acquisitions with the slit phantom translated in 1 mm increments perpendicular to the slit.

The system planar spatial resolution at 140 keV and 511 keV was evaluated using low and high energy collimators, respectively. The collimator parameters are given in Table 3-1. Line source images were acquired using 1 mm inner diameter capillary tubes containing either 500 μCi of $^{99\text{m}}\text{Tc}$ or 200 μCi of ^{18}F -FDG. Images with a minimum of 5.0×10^5 total counts were obtained at distances of 10 cm, 20 cm, and 30 cm from the collimator face and in both x and y orientations. Profiles were taken across the images to obtain line spread functions (LSFs) at each distance, and the FWHM was measured. For the 511 keV case, the FWHM was measured both with and without subtracting a constant from the LSF to reduce the effect of the septal penetration “tails” in the measured LSF. This constant, 0.18, was computed from the average intensity of twenty pixels not contained in the peak. The reported FWHM was the average of the x and y directions. These results were then compared to the theoretical FWHM calculated using the diameter of the collimator holes, d , depth of the holes, a , and the source-to-collimator distance, b (Fig. 3-1) [6]. Due to septal penetration, the effective length of collimator holes is somewhat less than their actual length. The effective length of collimator holes, a_{eff} , is given by [6]:

$$a_{\text{eff}} = a - 2\mu^{-1} \quad (3-1)$$

The spatial resolution of a parallel-hole collimator is given by [6]:

$$R_c = \frac{d}{a_{\text{eff}}} (a_{\text{eff}} + b) \quad (3-2)$$

Uniformity correction was applied to all the images acquired for spatial resolution measurements. The image used to uniformly correct each acquisition was the intrinsic flood image acquired for the energy resolution evaluation at the respective energy. A 40% energy window (only used counts with energies greater or less than 20% of 140 keV) was used for the 140 keV images and a 25% energy window was used for the 511 keV images.

The reconstructed SPECT spatial resolution at 140 keV was measured using a point source of ^{99m}Tc (2.5 mCi) located at the tip of a 1 cc syringe about 3 mm in diameter. A total of 19 projections (every 10° from 0° – 180°) with 5×10^5 counts per projection were obtained. The activity in the syringe was centered in the detector field-of-view with a radius of rotation of 22 cm. The projections were reconstructed using the maximum likelihood expectation maximum (MLEM) algorithm [7] with 50 iterations into a $46 \times 46 \times 46$ voxel image (5 mm^3 voxels). A profile was taken across a transaxial and coronal slice of the reconstructed image and from this, the FWHM was measured. The effect of projection angle sampling will be studied later, although it should be noted that the relatively small field-of-view relaxes the angular sampling requirement.

The reconstructed SPECT spatial resolution at 511 keV was measured using a point source of ^{18}F -FDG (200 μCi) located at the tip of a 1 cc syringe. As with the 140 keV case, 19 projections were obtained at every 10° from 0° – 180° with 1.0×10^5 counts per projection. The radius of rotation was 22 cm and the projections were reconstructed using MLEM [7] with 50 iterations into a $46 \times 46 \times 46$ voxel image (5 mm^3 voxels). Again, a profile was taken across a transaxial slice of the reconstructed image and from this, the FWHM was measured.

Detection Sensitivity

The extrinsic (with collimator) detection sensitivity in terms of $\text{counts} \cdot \mu\text{Ci}^{-1} \cdot \text{s}^{-1}$ was evaluated using point sources of 240 μCi ^{99m}Tc and 534 μCi ^{18}F -FDG suspended 30 cm from the

collimator face. A 600 s acquisition with a 40% energy window for ^{99m}Tc and a 25% energy window for ^{18}F -FDG was obtained for each source. The measured sensitivity was obtained by integrating the counts over the entire detector surface. An equation for detector sensitivity (g) is [6]:

$$g = \left(\frac{d}{a}\right)^2 \left(\frac{d}{d+t}\right)^2 \quad (3-3)$$

Count Rate Capability

The intrinsic detector count rate performance for 140 keV and 511 keV was evaluated using 1.1 mCi and 535 μCi of ^{18}F -FDG and ^{99m}Tc , respectively. Each source was suspended 30 cm from the detector face and 20 s acquisitions were obtained while the source decayed through several half lives. The counts per second (cps) minus background integrated over the entire detector surface were recorded at each time point. For this acquisition no out-of-field activity was used.

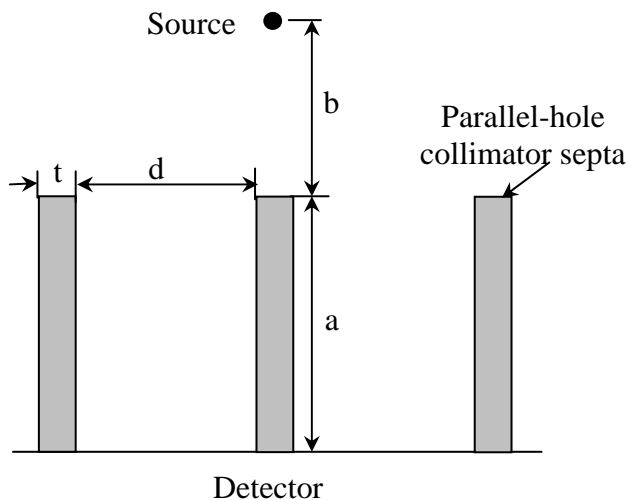


Figure 3-1. Cross-section of a parallel-hole collimator with different parameters labeled (not to scale).

Table 3-1. Low Energy (140 keV) and High Energy (511 keV) Collimator Parameters.

	Low Energy	High Energy
Hole Shape	hexagonal	hexagonal
Collimator Thickness [cm]	2.3	4.9
Hole Diameter [mm]	1.5	2.3
Septal Thickness [mm]	0.2	2.02

CHAPTER 4 SYSTEM EVALUATION RESULTS

Intrinsic Energy Resolution

The energy spectra from the ^{99m}Tc and ^{18}F -FDG images can be seen in Fig. 4-1. The measured FWHM was 45 keV (32%) for 140 keV and 117 keV (23%) for 511 keV. It is unclear at this time why the ^{99m}Tc spectrum contains negligible intensity to the left of the photopeak, unlike the ^{18}F -FDG spectrum in the figure and typical gamma camera spectra with ^{99m}Tc , but it is suspected that this is a result of the high voltage supply to the PMTs not being high enough to obtain counts from scattered 140 keV photons.

Spatial Resolution

The intrinsic spatial resolution was measured to be 5.6 mm FWHM at 140 keV and 6.1 mm FWHM at 511 keV. Fig. 4-2 shows the normalized LSFs from the slit phantom images. The suspected cause of the low intensity tails in the 511 keV LSF is from scatter in the tungsten box and in the PMTs.

Fig. 4-3 shows the normalized system spatial resolution LSFs from the capillary tube acquisitions at 140 keV and 511 keV. Each plot includes the measurements at 10, 20 and 30 cm from the detector face. For both energies, plots are shown for the x and y profile directions. The tails in the 511 keV LSFs are suspected to be from collimator septal penetration. Fig. 4-4 shows example line source images acquired at 10 cm from the detector face for both 140 keV and 511 keV.

Table 4-1 summarizes the measured FWHM as a function of distance from the collimator (“*b*”) including both with and without constant subtraction, the theoretical calculation and the percent deviation of the measured from the theoretical. The table shows that the tails from septal

penetration caused substantial increase in the measured FWHM and a closer agreement with the theoretical spatial resolution occurred after subtracting the constant.

To prove that the image degradation was actually a result of septal penetration and not scatter from surrounding materials, a simulation was run using the GATE software package [8], a front-end for the GEANT4 Monte Carlo simulation code [9], with the same geometry as the point source sensitivity acquisition but with no scattering material surrounding the crystal (for example, PMTs, gantry, and detector box).

Fig. 4-5 shows the acquired image A) and the simulated image B). The tails in the point spread function (PSF) from the simulated image show that the spread in the LSF resulted from septal penetration and not from scatter. An interesting observation is the difference in PSF and LSF at 511 keV. The height of the penetration tail is higher in the LSF (Fig. 4-3) due to the contribution of all parts of the line source to the tails in the profile. The point source does not have this extra source contribution at all points and therefore the tails are lower and only appear as a star pattern in the image.

Fig. 4-6 shows the reconstructed SPECT image of the 140 keV point source and the corresponding PSF obtained by integrating the intensity along columns in a transaxial and coronal slice from the image (and normalizing). The FWHM of the PSF was 1.59 cm in the transaxial direction and 1.57 cm in the coronal direction. This is in close agreement with the theoretical, planar system spatial resolution (1.57 cm), which is obtained from equation 4-2 with “*b*” equal to the radius of rotation used in the SPECT acquisition.

Fig. 4-7 shows the reconstructed SPECT image of the 511 keV point source and the corresponding PSFs in a transaxial and coronal slice. The FWHM of the PSF in the transaxial direction was 1.58 cm and 1.74 cm in the coronal direction. Again, this is in close agreement

with the theoretical, planar system spatial resolution (1.56 cm). Slight center of rotation artifacts are seen in the reconstructed slice that were not seen in the 140 keV case. These artifacts resulted from inaccuracies in detector rotation around the source due to the weight of the collimator and detector head. The weight made it hard to position the head exactly to completely eliminate center-of-rotation artifacts (see discussion in chapter 5).

Detection Sensitivity

From the total counts in the point source images, the detection sensitivity was calculated to be $3.1 \text{ counts} \cdot \mu\text{Ci}^{-1} \cdot \text{s}^{-1}$ for $^{99\text{m}}\text{Tc}$ and $1.89 \text{ counts} \cdot \mu\text{Ci}^{-1} \cdot \text{s}^{-1}$ for ^{18}F -FDG. The relative sensitivity with the two radionuclides can be accounted for by considering the relative geometric sensitivity of the low and high energy collimators and the relative efficiency of the detector to the 140 keV and 511 keV photons. The geometric sensitivity of the low energy collimator is a factor of 5 greater than that of the high energy collimator, using equation 3-3. The detection efficiency of the 12.5 mm NaI crystal to 140 keV photons is approximately a factor of 7 greater than that to 511 keV photons, using the attenuation coefficient of NaI. These two factors account for the increase in sensitivity for 140 keV photons. Overall, the measured sensitivity for 511 keV is much higher than expected, which is attributed to scattering in the tungsten box and the PMTs and septal penetration in the collimator.

Count Rate Capability

Fig. 4-8 shows plots of the detected count rate as a function of activity for $^{99\text{m}}\text{Tc}$ and ^{18}F -FDG. The maximum count rate of the detector was measured to be 1.46×10^5 cps for $^{99\text{m}}\text{Tc}$ and 1.56×10^5 cps for ^{18}F -FDG. At the time of the maximum count rate, there was 135 μCi of $^{99\text{m}}\text{Tc}$ present and 275 μCi of ^{18}F -FDG present. The saturation of the detector occurred at a lower activity for $^{99\text{m}}\text{Tc}$ because of the higher sensitivity of the detector at this energy. The images and energy spectra were distorted when the detector count rate was saturated.

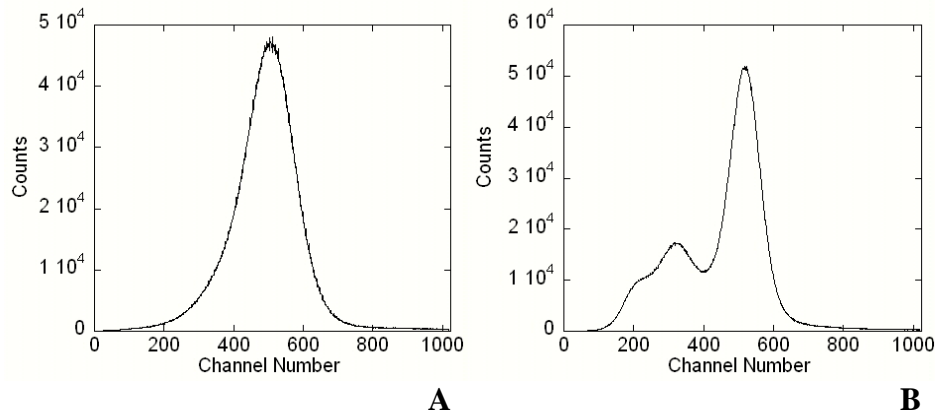


Figure 4-1. Energy spectra from flood images with two different point sources. A) ^{99m}Tc energy spectrum. B) ¹⁸F-FDG energy spectrum.

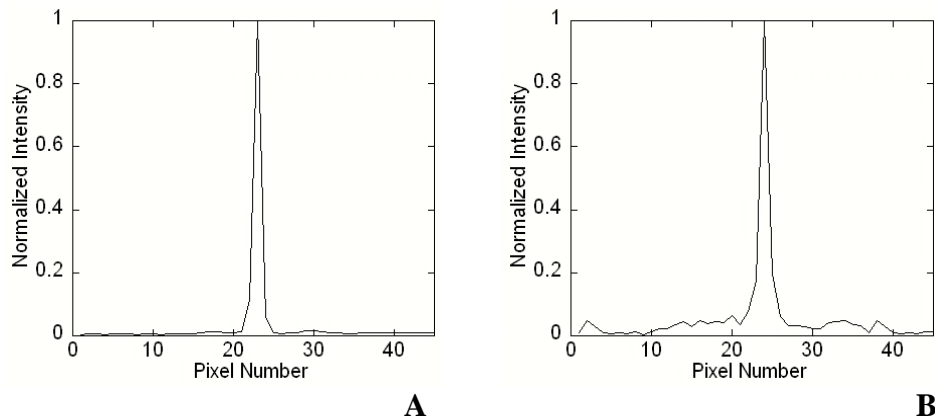


Figure 4-2. Normalized intrinsic spatial resolution LSFs. A) ^{99m}Tc LSF. B) ¹⁸F-FDG LSF.

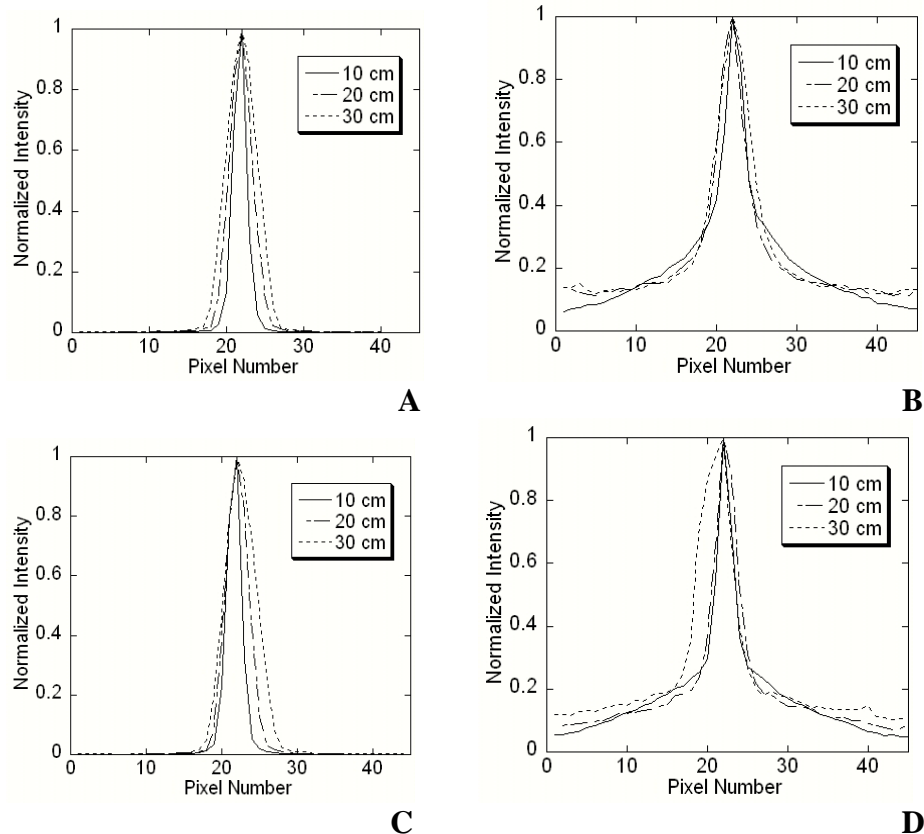


Figure 4-3. Normalized system spatial resolution LSFs at 10, 20, and 30 cm from the detector face in both the x and y directions. A) ^{99m}Tc LSF in the x direction. B) $^{18}\text{F-FDG}$ LSF in the x direction. C) ^{99m}Tc LSF in the y direction. D) $^{18}\text{F-FDG}$ LSF in the y direction.

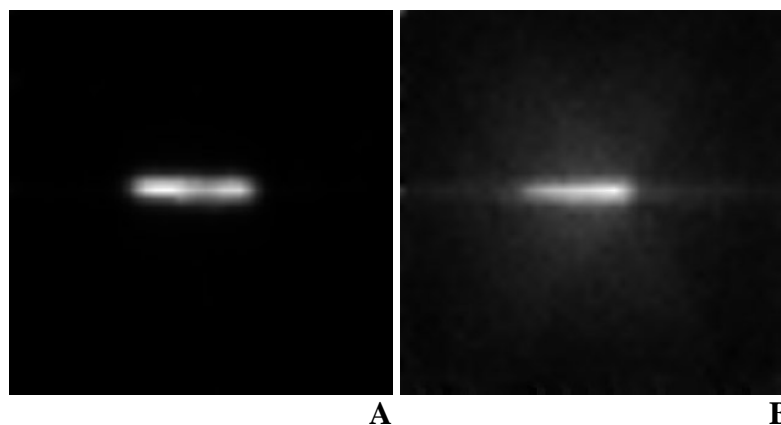


Figure 4-4. Line source images for system spatial resolution measurements. Line source to detector distance was 10 cm. A) ^{99m}Tc line source. B) $^{18}\text{F-FDG}$ line source.

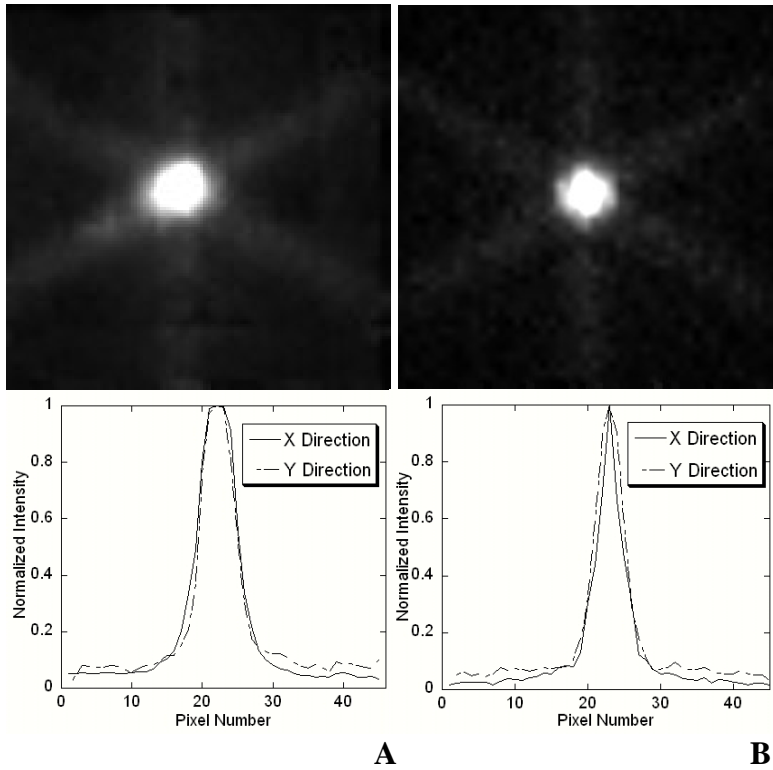


Figure 4-5. Acquired and simulated 511 keV point source images with the corresponding normalized PSFs in the x and y directions. A) Acquired point source. B) Simulated point source.

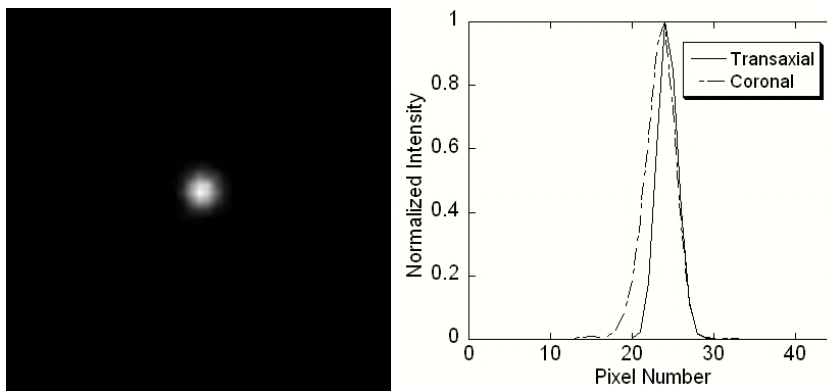


Figure 4-6. Reconstructed transaxial slice from a SPECT image from a ^{99m}Tc point source with its corresponding point spread functions in the transaxial and coronal directions.

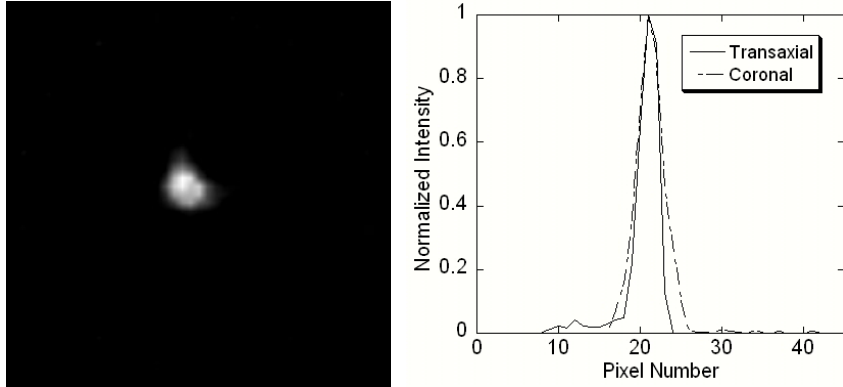


Figure 4-7. Reconstructed transaxial slice from a SPECT image from an ^{18}F point source with its corresponding point spread functions in the transaxial and coronal directions.

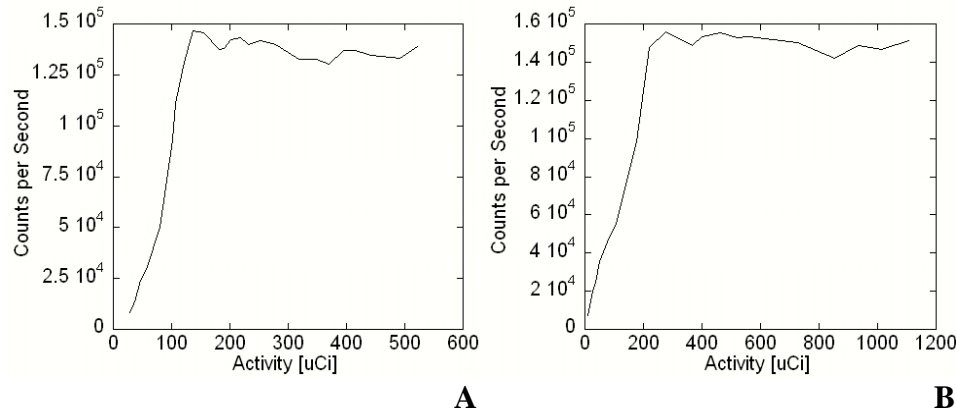


Figure 4-8. Count rate as a function of activity. A) $^{99\text{m}}\text{Tc}$ counting curve. B) ^{18}F -FDG counting curve.

Table 4-1. System Spatial Resolution (FWHM in cm).

Energy	b [cm]	Without subtraction	With subtraction	Theoretical	% Deviation
140 keV	10	1.14	N/A	0.99	14.7
	20	1.64	N/A	1.57	4.5
	30	2.35	N/A	2.18	7.8
511 keV	10	1.54	1.14	1.03	50.0 / 11.1
	20	1.93	1.62	1.56	23.7 / 3.8
	30	2.64	2.03	2.13	23.9 / -4.7

CHAPTER 5 DYNAMIC CARDIAC PHANTOM STUDIES

Introduction

To further the performance evaluation of the mobile system, a more realistic situation needed to be simulated. As stated earlier, one of the important needs of patients in an ICU environment is a cardiac viability study, since the patient cannot be moved to a traditional PET or SPECT facility. As a first anthropomorphic test for this system, a dynamic cardiac phantom (Model ECT/DY-CAR/P, Data Spectrum Corp. Hillsborough, NC, 27278), seen in Fig. 5-1, was used to simulate a patient confined to an ICU bed. The phantom contains a simulated liver, lungs, and spine, and the heart consists of two membranes with the simulated myocardium between them.

Methods

Four factors, angular sampling, counts per projection, cardiac motion, and out-of-field activity, were varied during acquisitions to determine how each would affect the reconstructed image. The reason for the different factors is that conditions in the ICU might call for shorter or longer acquisitions depending on the patient. The two major parameters affecting the length of an acquisition are number of projections and the number of counts per projection.

Each acquisition consisted of 21 projections, every 10° from 0 to 180° plus 45 and 135° . This allowed for reconstructions to be done with 19, 10, or 5 evenly spaced projections. Also, the number of counts per projection was varied from 5.0×10^5 , 2.5×10^5 , and 1.0×10^5 per projection. Approximately 1 mCi of activity was injected into the simulated myocardium for the acquisitions. For the out-of-field activity, an additional 1.2 mCi of activity was injected into the simulated liver. Projections were energy windowed to 20% to reject scatter. As an initial experiment, the first acquisitions with ^{99m}Tc were done with the heart positioned at end-systole

and end-diastole to remove any motion blur. Next, to simulate motion, the heart was pumped at 72 beats per minute (BPM) with an ejection fraction (EF) of 45% throughout the entire acquisition.

The projection data were reconstructed using MLEM (50 iterations) [7]. These were then filtered using a Hann filter (low pass) with a cut-off parameter of 1.1 cm^{-1} . As a metric to compare the quality of the images, profiles were taken across a coronal slice to obtain a ratio between the intensity in the myocardium to the intensity in the ventricle. Due to attenuation effects, one wall of the myocardium had higher intensity than the other so an average of the two walls was used for the myocardium intensity.

Results

Fig. 5-2 shows both the transaxial and coronal view of the end-systole and end-diastole $^{99\text{m}}\text{Tc}$ MLEM reconstructions at 2.5×10^5 counts per projection and 19 projections along with normalized coronal profiles. There is a slight distortion near the simulated apex of the myocardium because of an air bubble that was subsequently removed. The profile used in the coronal slice in Fig. 5-2 is the same used in determining the contrast ratio in the rest of the reconstructed images.

Table 5-1 contains the myocardium to ventricle intensity ratios for the motion acquisitions with 19, 10, and 5 projections with 5.0×10^5 , 2.5×10^5 , and 1.0×10^5 counts per projection. Secondly, to continue to assess the clinical feasibility of the system, activity was added into the simulated liver of the phantom to see if this resulted in any streaking artifacts in the reconstruction. Fig. 5-3 shows a transaxial and coronal slice from these acquisitions with 19, 10, and 5 projections and 2.5×10^5 counts per projection. The intensity ratios for the other out-of-field activity acquisitions are found in Table 5-1. As expected, the intensity ratio increased with number of projections and number of counts per projection.

We also want to be able to image patients using ^{18}F -FDG, so all of the previous $^{99\text{m}}\text{Tc}$ acquisitions will be repeated using ^{18}F -FDG. Due to the short half-life and the difficulty in obtaining ^{18}F -FDG, only the motion acquisitions with 2.5×10^5 and 1.0×10^5 counts per projection have been obtained to this point. Fig. 5-4 shows a transaxial and coronal slice from 2.5×10^5 count acquisitions at 19, 10, and 5 projections. The myocardium to ventricle intensity ratios from the other acquisitions are found in Table 5-1. The intensity ratios for the ^{18}F -FDG images are much lower than in the $^{99\text{m}}\text{Tc}$ images. This is due to artifacts from septal penetration in the collimator and uncorrected center-of-rotation errors due to the weight of the collimator. To improve the quality of the ^{18}F -FDG images, a center-of-rotation correction will have to be applied to the acquisitions. We have also considered applying a filter to the projection data to remove the effects of the septal penetration tails.

Discussion

The current protocol for obtaining a SPECT image uses a fixed ROR. There are two major problems with this method. First, spatial resolution improves as the collimator-to-object distance decreases. Therefore, as patients are not perfectly round, the spatial resolution is improved by placing the collimator as close to the patient as possible. The current protocol with a fixed ROR does not allow detector positioning like this.

Second, with a constant ROR, the detector head needs to be positioned exactly at the calculated horizontal (H) and vertical position (V) (equations 2-1 and 2-2) for each angle or the reconstruction will have center-of-rotation streaking artifacts (Fig. 2-7). The problem is that exact positioning is virtually impossible in the vertical direction with the 511 keV collimator because the weight of the collimator makes it hard to smoothly operate the vertical positioning motor. Vertical positioning can be obtained to within 1 cm but even this degree of accuracy can be difficult to achieve. Also, the heart is not positioned directly on the axis of rotation in the

anatomy, so some projections could potentially truncate some of the heart anatomy due to the small field-of-view of the detector. This means that it might be necessary to create a center-of-rotation shift to keep the heart in the field-of-view.

The solution to this problem is to develop an algorithm that would allow the detectors to be positioned in any orientation around the patient. This can be done by performing a center-of-rotation correction on the acquired projection images prior to the reconstruction to place them in the position they should be with the constant ROR protocol, which is required for image reconstruction. During an acquisition, both the actual position and angle of the head (from the digital protractor and gantry readout) and the required position and angle of the head for a constant ROR (from equations 2-1 and 2-2) are known. The algorithm will create an array of virtual 100×100 pixel detectors centered at the positions and angles where the heads would be with a constant ROR protocol, since these positions are needed for the reconstruction. Next, the actual detector head is positioned at the same projection angle and the virtual detector, but as close to the patient as possible and with the heart anatomy in the field of view to ensure no truncation of anatomy. The location of the head is recorded from the digital readout on the gantry and the image is acquired. This image is then projected onto the 100×100 virtual detector head. By using the actual location of the detector and the location of the center of the virtual detector, the acquired image can be shifted to the center of the virtual detector. This is the location the detector would have been at if a constant ROR protocol was used. The shift is performed on all projections and the final image can be reconstructed without center-of-rotation artifacts or truncation of heart anatomy. Fig. 5-5 illustrates several possible detector positions at $\theta = 45^\circ$. Any of the images could easily be projected onto the virtual detector located at the fixed ROR location and shifted to the center position, eliminating center-of-rotation artifacts.

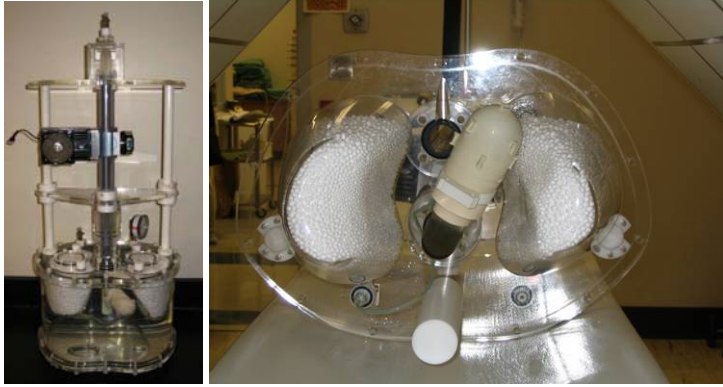


Figure 5-1. Dynamic cardiac phantom with simulated myocardium, lungs, spine, and liver.

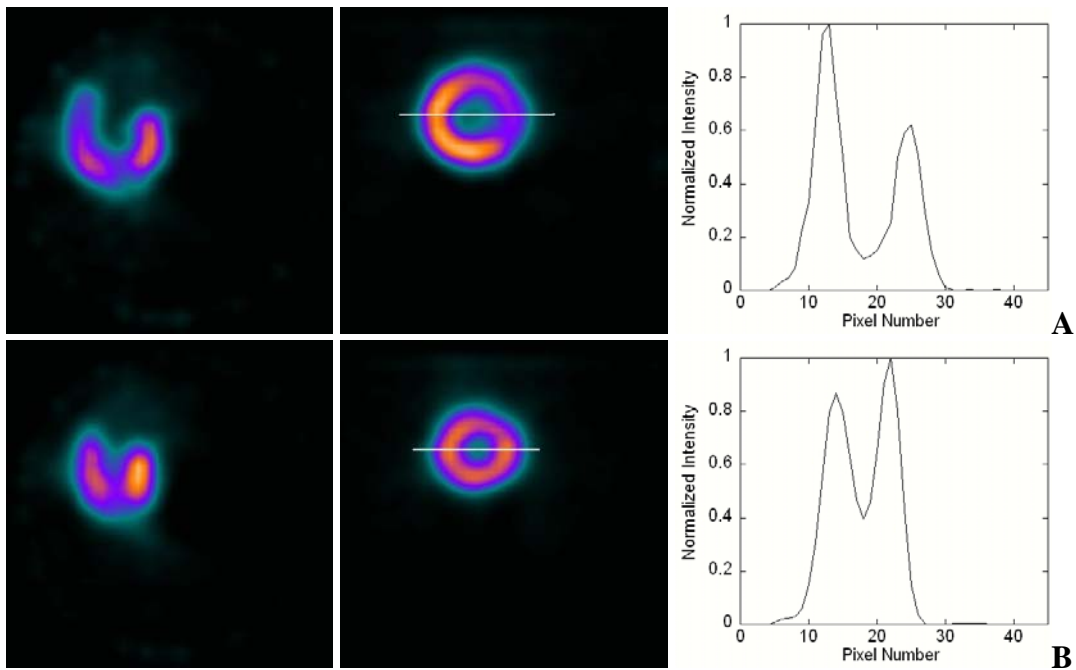


Figure 5-2. ^{99m}Tc end-diastole and end-systole reconstructions from 19 projection angles and 2.5×10^5 counts per projection with the corresponding profile. A) End-diastole reconstruction. B) End-systole reconstruction.

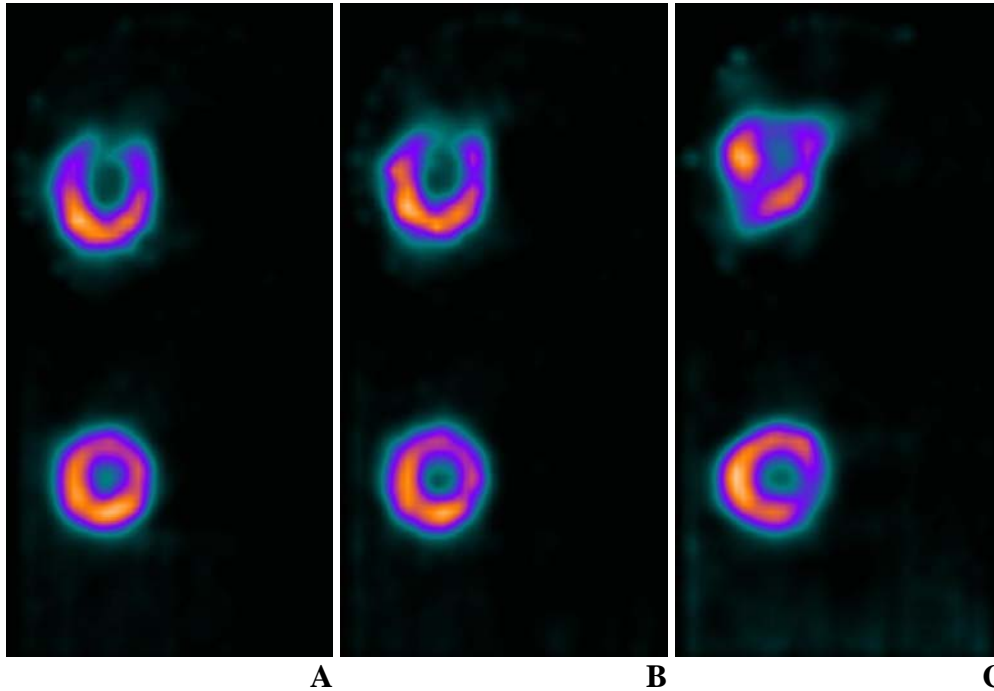


Figure 5-3. Transaxial and coronal slices using ^{99m}Tc with varying number of projection angles with 2.5×10^5 counts per projection with both cardiac motion and out-of-field activity in the liver. A) 19 projection angles. B) 10 projection angles. C) 5 projection angles.

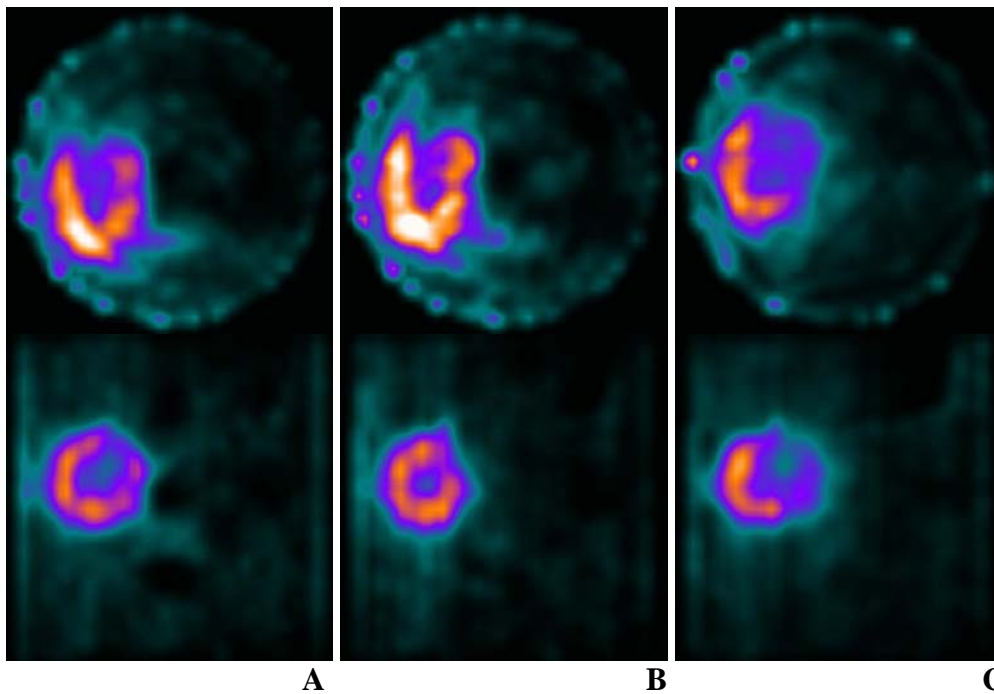


Figure 5-4. Transaxial and coronal slices using ^{18}F -FDG with varying number of projection angles with 2.5×10^5 counts per projection with cardiac motion, only. A) 19 projection angles. B) 10 projection angles. C) 5 projection angles.

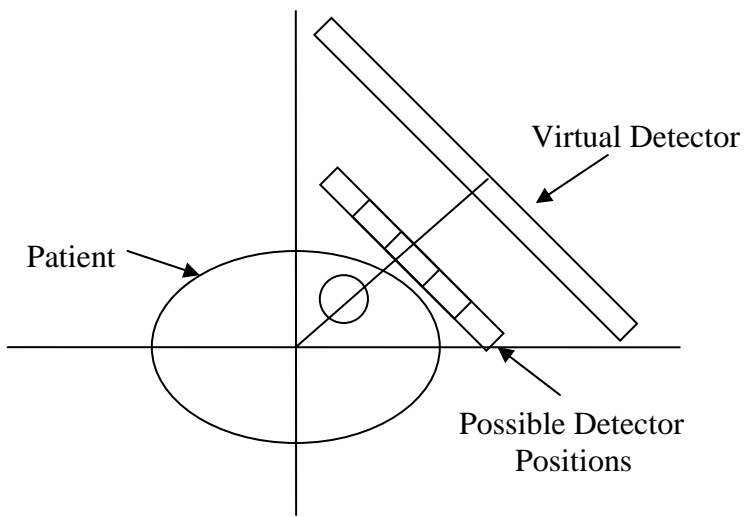


Figure 5-5. Projection at $\theta = 45^\circ$ showing that the detector can be located at any position to achieve the best image while at the same time eliminating center-of-rotation artifacts and truncation of anatomy.

Table 5-1. Myocardium to Ventricle Intensity Ratios for Different Acquisition Parameters.

		Cardiac Motion			Cardiac Motion with Out-of-Field Activity		
	# projections	1.0×10^5	2.5×10^5	5.0×10^5	1.0×10^5	2.5×10^5	5.0×10^5
^{99m}Tc	19	4.98	5.56	6.73	4.80	4.84	4.90
	10	4.96	4.98	5.57	3.94	4.43	4.83
	5	3.87	4.01	4.00	3.15	2.75	3.32
$^{18}\text{F-FDG}$	19	1.98	1.76	-	-	-	-
	10	1.90	2.10	-	-	-	-
	5	1.52	1.60	-	-	-	-

CHAPTER 6 CONCLUSIONS AND FUTURE WORK

The system was evaluated for imaging both ^{99m}Tc and ^{18}F -FDG emitters based on energy resolution, spatial resolution, detection sensitivity and count rate capability. The ability to use both radiotracers makes this system very versatile. The performance generally matched the theoretical predictions and demonstrated promise for effectively performing bedside cardiac SPECT imaging in settings such as an intensive care unit or an emergency room. Dynamic cardiac phantom studies further supported the fact that cardiac imaging is possible. Acquisitions showed that higher counts per projection and more projection angles increase the myocardium to ventricle intensity ratio in the images, but if the situation requires a faster acquisition with less projection angles, this system can still provide a viable image. Future work will involve finishing the ^{18}F -FDG dynamic cardiac phantom acquisitions and progressing onto patient imaging. The algorithm correcting for center-of-rotation error in ^{18}F -FDG acquisitions will continue to be developed and implemented. We will also look into filtering of the ^{18}F -FDG acquisitions to lower the effect of septal penetration. Future work will also involve evaluating PET imaging performance.

LIST OF REFERENCES

1. Mabuchi, M., N. Kubo, K. Morita, K. Noriyasu, Y. Itoh, C. Katoh, Y. Kuge, N. Tamaki, "Value and Limitation of Myocardial Fluorodeoxyglucose Single Photon Emission Computed Tomography using Ultra-high energy Collimators for Assessing Myocardial Viability." *Nuclear Medicine Communications*, 2002; 23:879:885.
2. Matsunari, I., T. Yoneyama, S. Kanayama, M. Matsudaira, K. Nakajima, J. Taki, S.G. Nekolla, N. Tonami, K. Hisada, "Phantom Studies for Estimation of Defect Size on Cardiac ^{18}F SPECT and PET: Implications for Myocardial Viability Assessment." *Journal of Nuclear Medicine*, 2001; 42:1579-1585.
3. G. Weisenberger, S. Majewski, D. Gilland, W. Hammond, B. Kross, V. Popov, J. Proffitt, J. McKisson, and M. F. Smith. "Implementation of a Mobile, Cardiac PET Imager for the Emergency Room and Intensive Care Unit." 2007 IEEE Nuclear Science Symposium and Medical Imaging Conference.
4. Raylman, R. R., S. Majewski, M. F. Smith, R. Wojcik, A. Weisenberger, B. Kross, V. Popov, J.J. Derakhshan, "Comparison of Scintillators for Positron Emission Mammography (PEM) Systems." *IEEE Transactions on Nuclear Science*, 2003; 50:42-49.
5. Tipnis, U., Smith, M. F., Turkington, T. G., Wilson, J., Majewski, S., Gilland, D. R. "A Simulation Study of a Bedside Cardiac PET Imager." 2004 IEEE Nuclear Science Symposium Conference Record, 16-22 Oct, 2004, vol. 5, pp. 3126-3129.
6. S. Cherry, J. Sorenson, M. Phelps, "Physics in Nuclear Medicine." 3rd ed. Philadelphia: Saunders, 2003.
7. Shepp, L. A., Vardi, Y. "Maximum Likelihood Reconstruction in Positron Emission Tomography." *IEEE Trans. Medical Imaging*, 1 (2), 113-122, 1982.
8. S. Jan, G. Santin, D. Strul, S. Staelens, K. Assié, D. Autret, *et al.*, "GATE: A Simulation Toolkit for PET and SPECT." *Physics in Medicine and Biology*, 2004; 49:4543-4561.
9. Geant4 Collaboration, "GEANT4: A Simulation Toolkit." *Nuclear Instruments and Methods in Physics Research*, 2003; NIM A 506:250-303.

BIOGRAPHICAL SKETCH

Matthew Thomas Studenski was born in Royal Oak, Michigan, on May 27, 1983.

Matthew received his Bachelor of Science degree in 2005 from the University of Michigan–Ann Arbor in nuclear engineering and radiological sciences. In 2006, he received his Master of Science degree from the University of Michigan–Ann Arbor in nuclear engineering and radiological sciences. He is currently pursuing a PhD at the University of Florida in medical physics with Dr. David Gilland. Matthew's focus is primarily on nuclear medicine and imaging applications.

While finishing his master's degree at the University of Michigan with Dr. Kimberlee Kearfott, Matthew published two articles: (1) Design and Simulation of a Neutron Facility. *Health Physics. Operational Radiation Safety*. 92(2) (Supplement 1): S37-S44, February 2007. and (2) Simulation, Design, and Construction of a Cs-137 Irradiation Facility. *Health Physics. Operational Radiation Safety*. 92(5) (Supplement 2): S78-S86, May 2007.